Fabrication of sub-20 nm MoS$_2$ horizontal nanowire on silicon substrates by inclusion of precursors into polystyrene-b-polyethylene oxide nanopatterns: Detailed structural investigation

Tandra Ghoshal (✉) and Michael A. Morris (✉)

School of Chemistry, AMBER and CRANN, Trinity College Dublin, Dublin, Ireland, D02 AK60

ABSTRACT

Herein, we demonstrate the fabrication of sub-20 nm MoS$_2$ horizontal nanowire arrays on silicon substrates using a self-assembled block copolymer assisted *in situ* inclusion approach. Microphase separated long-range ordered polystyrene-b-polyethylene oxide (PS-b-PEO) block copolymer (BCP) line-space nanopatterns were achieved through thermo-solvent annealing. The patterns produced had long-range order and domain sizes > 1 μm. The BCP structures were lightly etched and modified by anhydrous ethanol to facilitate insertion of molybdenum precursor within the film maintaining the parent BCP arrangements. Horizontal ordered molybdenum oxide nanowire arrays were then fabricated by ultraviolet (UV)/ozone treatment at room temperature. The oxides were converted to sulphides by thermal evaporation at different temperatures in Ar/H$_2$ environment. X-ray photoelectron spectroscopy revealed the composition and phases of the molybdenum oxide and sulphide nanowires. Elemental mapping was performed to investigate the interfaces between the oxide and sulphide nanowires with the substrate surface. The formation and stability of the sulphide nanowires were studied at different temperatures. The photoluminescence and Raman properties were studied at different formation temperatures to investigate defects and estimate the number of layers.

KEYWORDS

MoS$_2$, block copolymer, nanowires, inclusion, X-ray photoelectron spectroscopy (XPS), mapping, photoluminescence

1   Introduction

Recent advances in the fabrication of ultrathin monolayered materials have enabled investigations of new low-dimensional physics such as massless Dirac fermions and anomalous quantum Hall effects [1, 2]. Two-dimensional (2D) materials hold particular interest in this regard. MoS$_2$ is a typical example, a member of layered transition metal dichalcogenide family of materials. Bulk MoS$_2$ is semiconducting with an indirect bandgap of 1.2 eV, whereas it changes to a direct gap of 1.8 eV in monolayer form [3]. MoS$_2$ in nanotube and nanowire forms is also interesting for its electronic and optical properties due to quantum mechanical confinement [4, 5]. However, the formation of dense arrays of MoS$_2$ nanowires on substrates for potential use in integrated circuits and other electronic nanowires is challenging and remains an objective; the deposition and organization of preformed MoS$_2$ nanotubes or nanowires at substrates seem unlikely in structures consistent with dense device fabrication [6–9]. An alternative approach may be patterning of molybdenum oxide (MoO$_3$) and sulfurization to form arrays. MoO$_3$ is a relatively inexpensive n-type semiconductor material widely used as a catalyst for partial oxidation of hydrocarbons or for selective catalytic reduction of NO$_x$ [10]. Also, it has been used in the field of gas sensing, solid lubricants, electrochromic applications and as an anode in Li-ion battery technology [11].

Formation of dense nanowire arrays for nanodevices can be achieved by photolithography and chemical-based self-assembly is an attractive approach for creating nanowires with complex chemistries. Generally, dense nanowires can be prepared by several bottom-up techniques and need to be organised into the desired device setting, which remains a challenge though significant progress has been made [12, 13]. Among different nanofabrication bottom-up methods, directed self-assembly (DSA) of microphase-separated structures of block copolymer (BCP) is considered favourable for its high throughput, low cost and simplicity for generating line and space shaped patterns on substrates [6, 14–16]. The nanowires prepared by this BCP approach do not require further steps to arrange themselves for the nanodevice applications. However, there are still several challenges such as defects, controllability and self-assembly kinetics for wider applications of the BCP [17]. We have previously investigated this approach for development of MoS$_2$ nanowires on silicon using a polystyrene-b-polyvinylypyridine (PS-b-P4VP) system. Herein, we extend these studies towards an alternative BCP template, PS-b-PEO, investigating in more depth the formation of the nanowires and studying their optical properties. A key advantage of the improved methodology here is the use of a cylinder BCP system since the alignment (orientation to the surface plane) of line-space patterns is easier compared to lamellar systems since control of the interfacial interactions is less problematical [18]. Further, we are able to produce patterns with

---

very high order and domain sizes in excess of a micron. This allows us to carry out in depth characterisation due to the regularity of the patterns and the feature sizes. These structures are amenable to material modification because both blocks are present at the surface. MoO_3 nanowire arrays are realized by an established *in-situ* selective inclusion (into the BCP patterns) methodology [19, 20]. Low-temperature sulfurization converts [21] MoO_3 into MoS_2 without disturbing the parent nanowire pattern revealing significant integrity with the substrate [22].

This report is of significance combining simplicity, controllability (morphology and orientation of BCP) and cost using self-assembly with an "*in-situ*" inclusion technique followed by ultraviolet (UV)/ozone treatment to generate MoO_3 and MoS_2 horizontal nanowire arrays. The morphology, interfaces and elemental composition of the arrays were systematically studied using scanning electron microscopy (SEM), cross-sectional transmission electron microscopy (TEM), X-ray photoelectron spectroscopy (XPS) and elemental mapping. Photoluminescence and Raman measurements were also performed for defect-related studies on the samples synthesized at different temperatures.

2 Results and discussion

In this report, we have used a cylindrical phase forming PS-b-PEO, yielding a morphological arrangement of PEO cylinders inside a PS matrix after solvent mediated microphase separation. The spin-cast films were exposed to different annealing solvents, temperatures and time to achieve the desired structural arrangement and orientation of the PEO cylinders with minimal defects. The solvents used were toluene and tetrahydrofuran (THF). Cyclical flipping of cylinders or local disordered and/or mixed orientation was realized when using either toluene or THF solely at different temperatures and annealing time [22, 23]. It is seen that a 1:1 volume ratio of toluene/THF mixture (in separate reservoirs) at annealing temperature of 50 °C for 3 h provides almost defect-free parallel orientation of PEO cylinders in PS matrix. Figures 1(a) and 1(b) show the representative atomic force

microscopy (AFM) and SEM images of the BCP after exposure to this solvent respectively. The AFM image in Fig. 1(a) indicates ordered parallel cylindrical arrangements without de-wetting. The SEM image (Fig. 1(b)) also indicates similar structural arrangements of PS and PEO microdomains despite their similar densities and average atomic number. The film surface is at uniform level with a thickness of around 42 nm as measured by ellipsometry. The average measured centre-to-centre cylinder distance is 42 nm with a cylinder diameter of 19 nm.
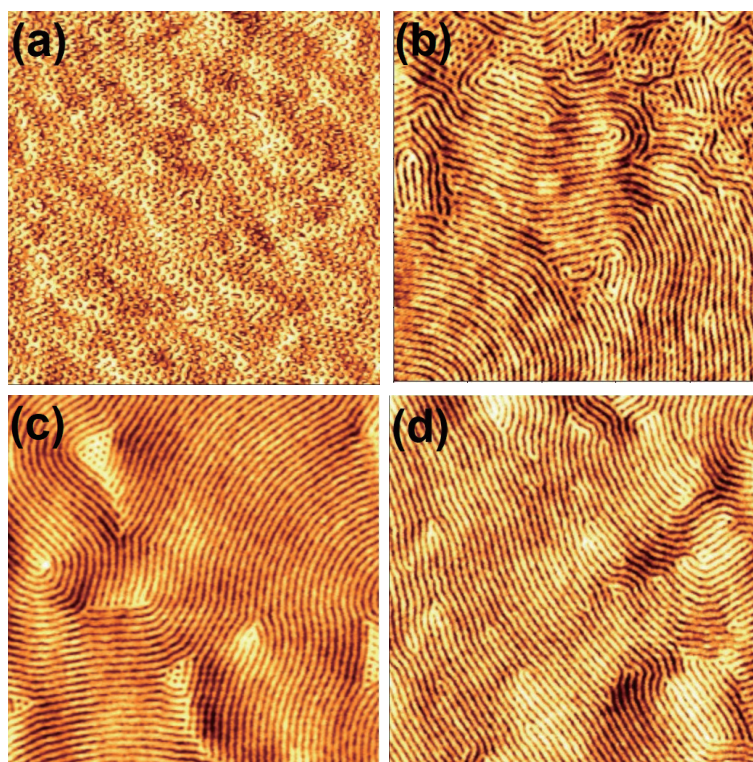
The morphological evolution of the films with annealing time when other processing conditions remained unchanged is shown in Fig. 2. 30 min exposure forms perpendicularly orientated PEO cylinders across the whole substrate. Film thickness undulations and non-uniform feature sizes are also realised (Fig. 2(a)). Figure 2(b) shows mixed perpendicular and parallel orientations of the cylinder across the wafer at an annealing time of 1 h. The average measured centre-to-centre cylinder distance and diameter are uniform and similar for both orientations. The parallel cylindrical orientation dominates at 1.5 h (Fig. 2(c)) annealing time but is accompanied by formation of small islands with perpendicular cylinders. This is related to non-uniform thickness of the film (± 2 nm). The parallel-only cylinder orientation was achieved as the annealing time increased to 2 h (Fig. 2(d)). The average measured centre-to-centre cylinder distance is the same as before (42 nm a diameter 19 nm). However, large domain sizes (> 1 μm) with good long-range ordered, uniform thickness and cylinder diameter were realized only after 3 h annealing (Figs. 1(a) and 1(b)). The high periodicity of these patterns is significantly greater than the observed previously [24] and allows much better characterization because of their regularity.

Here, toluene and THF are used together to affect microphase separation. Toluene and THF are selective solvents for PS, since the solubility parameter difference of toluene with PS is much smaller ($|\delta_{Tol} - \delta_{PS}| = |18.3 - 18| = 0.3$ MPa$^{1/2}$) than that with PEO ($|\delta_{Tol} - \delta_{PEO}| = |18.3 - 20.2| = 1.9$ MPa$^{1/2}$). Similarly, the solubility parameter difference of THF with PS is ($|\delta_{THF} - \delta_{PS}| = |18.5 - 18| = 0.5$ MPa$^{1/2}$) is also smaller than with PEO ($|\delta_{THF} - \delta_{PEO}| = |18.5 -$
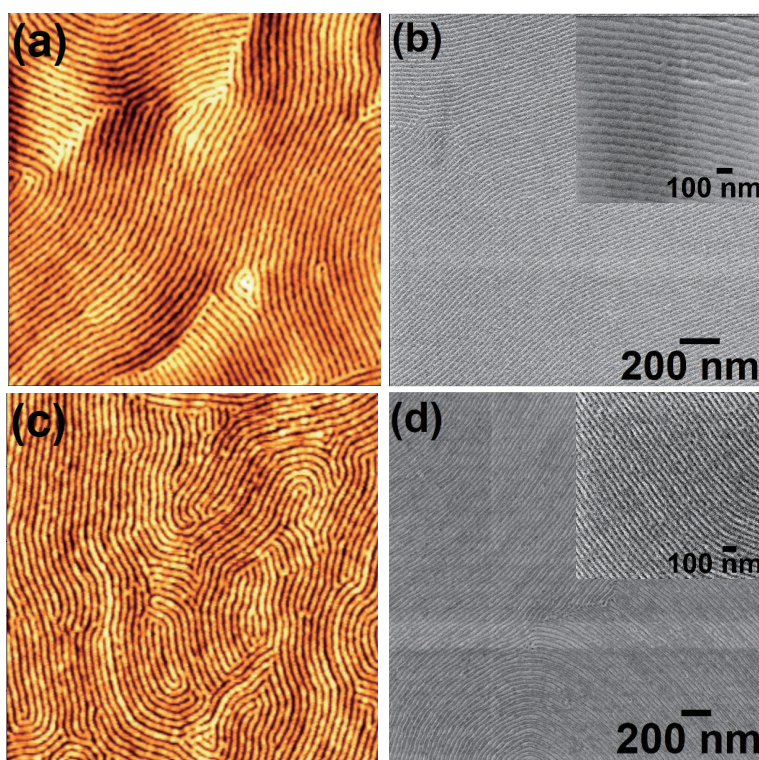
Figure 1 Representative topographical ((a) and (c)) AFM and ((b) and (d)) SEM images of the PS-b-PEO (42k–11.5k) after microphase separation in toluene/THF mixture at 50 °C for 3 h and ethanol treatment at 40 °C for 16 h respectively. Insets of (b) and (d) show the corresponding magnified images.

Figure 2 AFM images of the films annealed in toluene/THF mixture at 50 °C with the annealing time of (a) 30 min, (b) 1 h, (c) 1 h 30 min and (d) 2 h respectively, showing the morphological evolution.

20.2| = 1.7 MPa$^{1/2}$). Short-period solvent annealing gives a vertical orientation because this represents the least entropically hindered route to microphase separation, as the PEO cylinder length is limited to the thickness of the films. However, at extended time periods the cylinders can relatively easily re-orientate parallel to the substrate surface less favoured entropically when this orientation is thermodynamically favoured. This occurs at the exact monolayer film thickness (used here) as this ensures the PEO cylinders only have a PS interface. With other non-monolayer film thicknesses, thermodynamics is less favourable for the parallel orientation [25]. This thickness variation at shorter annealing time may result from spin-coating and/or trapped solvent. Solvents can be trapped in the film because of vitrification of the film during solvent removal [26]. This can "freeze-in" both film irregularities as well as solvent swelling thickness changes. The increased order and the uniformity of pattern orientation for the longer annealing time are probably due to increased film smoothness.

The microphase separated PS-b-PEO thin films with parallel cylinder orientation were used as a template to prepare molybdenum oxide and sulphide nanowire arrays by *in-situ* inclusion methodology as reported previously by our group [19–24, 27–30]. PEO microdomains were used for selective incorporation of metal ions into the template. This is realised by etching and/or modification of the PEO site through immersing the film in anhydrous ethanol at 40 °C for 16 h. Structural arrangement, dimensions and ordering remain unchanged after the treatment. The AFM and SEM images (Figs. 1(c) and 1(d)) show some increase in the phase contrast after this treatment, indicating etched/modified PEO microdomains. The higher magnification SEM image in the inset of Fig. 1(d) is consistent with this partially porous structure. No thickness change of the polymer film was observed after ethanol treatment. The ethanol treatment is a pre-requisite to form well-defined oxide nanopatterns described as an "activation step". It was also important to dry the films and carry out cation inclusion as quickly as possible presumably to minimize adventitious water

uptake. Longer exposure to ethanol and higher temperatures resulted in structural degradation.

Oxide nanowires are formed by our established *in-situ* inclusion methodology [27, 28, 30] that incorporate the metal ions into the PEO component via spin coating of the precursor solution. Ordered large-area molybdenum oxide nanowire arrays are realized with uniform size/shape and an arrangement that mimics the original BCP patterns (Fig. 3(a)). The inset of Fig. 3(a) shows the average diameter of the nanowires is 16 nm (a small contraction compared to that of as-synthesised BCP films) and is equal throughout the entire length. The PS matrix excludes the possibility of the ethanol mediated metal ion inclusion because of its hydrophobic nature. The similarity of the chemical structures of PEO monomers [(CH$_2$CH$_2$O)-] and ethanol molecules (H-CH$_2$CH$_2$O-H) is important and ethanol is highly effective in swelling the PEO domains and allowing infiltration. Intra or intermolecular coordination chemistry between metal ions and PEO via electron donation from the PEO block is also important for effective inclusion [31, 32]. Considering the fact that spin coating was performed for just a few seconds, diffusion through the pores and enrichment of the solid inside the pores must be a rather rapid process. The effectiveness of this simple solution mediated inclusion supports the suggestion that the ethanol activation step does not involve PEO removal and that PEO is present at the surface [28]. Complete removal of the PEO was achieved during the ethanol activation step, it would be highly unlikely that significant amounts of metal uptake and controlled selected area placement would have occurred because the PS matrix would be hydrophobic and the concentration of metal in solution is rather low.

The chemical composition of the molybdenum oxide nanowires after UV/ozone treatment was confirmed by XPS studies. A typical XPS survey spectrum (Fig. 3(b)) of molybdenum oxide nanowires confirms the expected presence of Si, O, C and Mo. The C 1s signal is relatively small, which demonstrates effective removal of carbon species during processing. Its intensity is consistent with those of adventitious material formed by
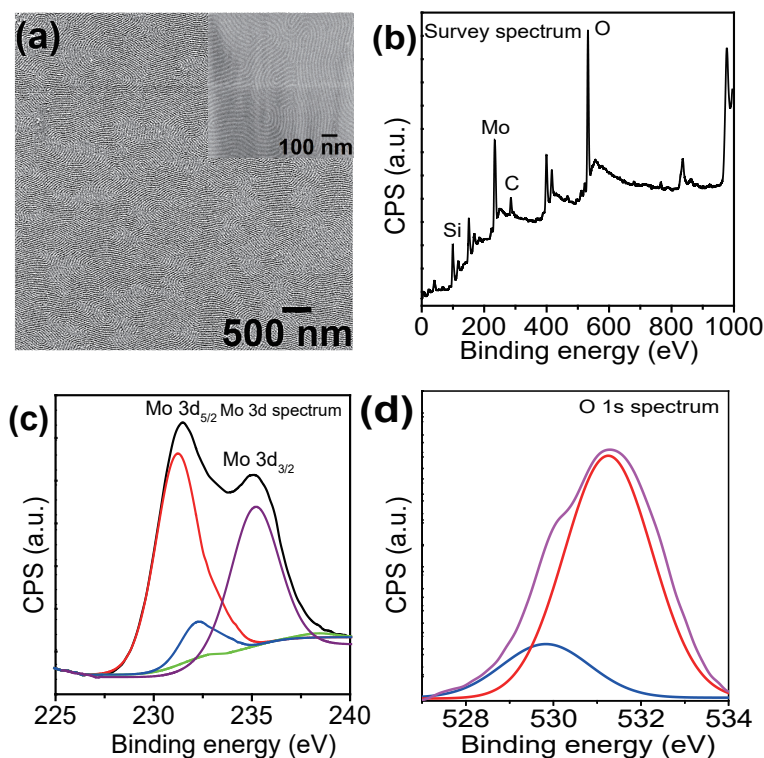
Figure 3 (a) SEM images of MoO₃ nanowires after spin-coating precursor-ethanolic solution onto the modified template followed by UV/ozone treatment at room temperature. (b) Survey, (c) Mo 3d and (d) O 1s XPS spectra of MoO₃ nanowires respectively.

adsorption and other contamination during sample preparation. Mo 3d high-resolution XPS spectra are shown in Fig. 3(c). The spectrum shows two well resolved spectral lines at 231.5 and 235.3 eV, which are assigned to Mo $3d_{5/2}$ and Mo $3d_{3/2}$ spin–orbit components respectively [33]. These values are in good agreement with the polycrystalline form of MoO₃ and suggest that the as formed nanowires are polycrystalline [34, 35] The spectra show no evidence of splitting or broadening within the resolution of the instrument, indicating the Mo was present in a single environment. The XPS O 1s spectrum shown in Fig. 3(d) shows a slightly broadened peak. Gaussian-Lorentzian curve-fitting provides individual binding energies of 529. 8 and 531.1 eV. The majority high intense peak at 531.1 eV is related to oxygen species reacted with metal and related to oxidation state of MoO₃ [36]. The small intense peak corresponds to Si–O bond originated from the exposed Si substrate.

Figure 4(a) shows the SEM image of the sulfurized nanowires. The well-separated nanowires remain intact at the substrate surface after sulfurization. Long range ordered uniform diameter nanowires were realized after the transformation. The average diameter of the nanowires is 15 nm and equal throughout the entire length with a centre-to-centre nanowire distance of 42 nm as the parent BCP structure. Thus, sulfurization process does not affect the structure and morphology of the BCP. The chemical composition of the molybdenum sulphide nanowires was confirmed by XPS studies. A typical XPS survey spectrum (Fig. 4(b)) of molybdenum sulphide nanowires confirms the expected presence of Si, S, O, C and Mo. The C 1s signal is consistent with that of adventitious material. The chemical composition of the molybdenum sulphide nanowires was confirmed by Mo 3d high-resolution XPS spectrum shown in Fig. 4(c). The spectrum showed two Mo 3d spin–orbit coupled contributions at 230.2 and 233.3 eV, which are assigned to Mo $3d_{5/2}$ and Mo $3d_{3/2}$ respectively. These peak positions are reflective of the semiconducting behaviour of MoS₂ (2H-MoS₂) [37, 38]. The S 2p high resolution XPS spectrum shows two well-resolved peaks at 162.6 and 163.9 eV, which are assigned to S $2p_{3/2}$ and $2p_{1/2}$ in the

2H-MoS₂ phase respectively as shown in Fig. 4(d) [39]. The Mo and S are present in the 1:2 atomic ratio and also suggest the formation of MoS₂. In addition to the main features, a new small peak is located at a higher binding energy (235.3 eV), which is ascribed to Mo⁶⁺, probably due to surface oxidation of the nanowires [39]. The XPS O 1s spectrum shown in the inset of Fig. 4(d) showed a symmetrical peak at binding energy of 529.8 corresponding to the Si–O bond from the exposed substrate between the nanowires.

The precise structural arrangement, positions and interfaces of the Si, silica and molybdenum oxide nanowires were obtained from high resolution EDAX mapping. A carbon layer was deposited on top of the oxide nanowires as a protecting layer during FIB lamellae preparation to enhance the contrast between nanowires. No defects or delamination was observed at the interface between the substrate and the nanowires reflecting the bonding, efficiency and structural integrity of the nanowires during FIB processing. Figure 5(a) shows well separated, uniform diameter ordered nanowires on the substrate surface. The nanowires have a compressed hemispherical shape and may reflect the spherical cross-section of the PEO domains of the BCP. No agglomerated or irregular diameter nanowires can be seen. The diameter of the nanowires was around 16 nm with an average height of 4 nm. The higher magnification image shown in Fig. 5(b) confirms that the nanowires were thicker at the middle in comparison to the sides. They were residing on a thin native oxide layer on the Si substrate. Elemental composition was confirmed by high resolution EDAX mapping and the distributions of Mo, O and Si are shown in Figs. 5(c) and 5(d). The STEM image again confirms the shape and sharp interfaces of the nanowires on the substrate. Figure 5(c) shows a homogeneous distribution of Mo corresponding to each nanowire and a sharp elemental interface to the substrate surface, suggesting no inter-diffusion occurs. The O and Si maps confirm the presence of oxides on the nanowire and passive layer and the substrate respectively.

Similarly, the structural arrangement, positions and interfaces
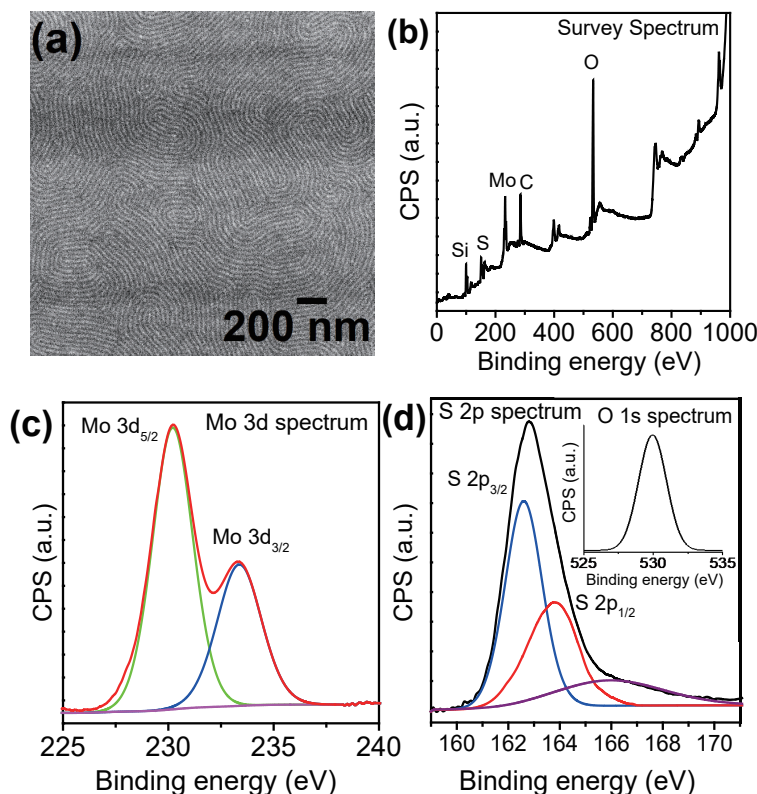
Figure 4 (a) SEM images of MoS$_2$ nanowires formed by thermal evaporation of sulphur powder at 450 °C in an Ar/H$_2$ gas flow. (b) Survey, (c) Mo 3d, and (d) S 2p XPS spectra of MoS$_2$ nanowires (inset is O 1s XPS spectrum).
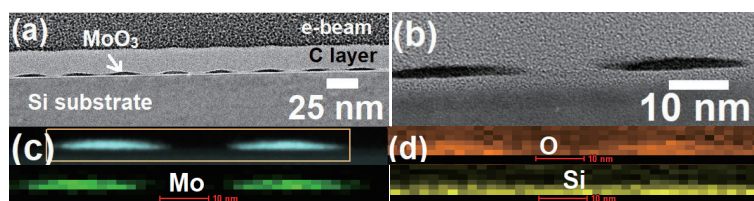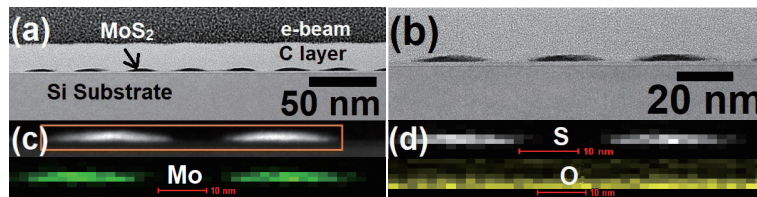

Figure 5 (a) and (b) Cross-sectional TEM images of MoO$_3$ nanowires on Si substrate. (c) and (d) STEM and elemental mapping of MoO$_3$ nanowires.

of the Si, silica, and converted molybdenum sulphide nanowires were also obtained from high resolution EDAX mapping. Similar processing steps were followed for the lamellae preparation. Well ordered MoS$_2$ nanowires with uniform diameter were noticed, as shown in Figs. 6(a) and 6(b). The average diameter of the nanowires is 15 nm with centre–centre spacing of 42 nm. The shape and sharp interfaces confirm these have been converted from the MoO$_3$ nanowires without any structural defect. Elemental composition was confirmed by high resolution EDAX mapping and the distributions of Mo, O and S are shown in Figs. 6(c) and 6(d). The mapping was realized for two of the nanowires as shown by the STEM image (Fig. 6(c), top)). The map (Fig. 6(c), bottom)) shows a homogeneous distribution of Mo corresponding to each nanowire and a sharp elemental interface to the substrate surface suggesting no inter-diffusion occurs. The S map (Fig. 6(d), top)) confirms the formation of sulphide nanowires. No oxides (Fig. 6(d), bottom)) were detected on the nanowires and complete conversion of the oxides to sulphides was confirmed. The oxide was present only on the passive layer on the substrate surface.

The stability of the MoS nanowire arrays was examined through the conversion process by varying the sulfurization temperature while keeping all other parameters unchanged. Figures 7(a) and 7(b) show the SEM images of the sulfurized nanowires prepared at 550 and 650 °C for 1 h respectively. Both of the images reveal well-attached and arranged MoS$_2$ nanowires on the substrate though the thermal decomposition temperature of the nanowires was reported as 650 °C [40]. The MoO$_3$ nanowires

were formed by *in-situ* inclusion process either intra- or intermolecular coordination of PEO with the metal ions followed by a slow UV/ozone treatment to remove any solvent, oxidize and cross-link metal ions forming oxide and remove the organic part simultaneously. This process leads to robust attachment of the oxide with the substrate [28]. MoS$_2$ nanowires formed by sulfurization through the evaporation of sulphur powder which reacts with MoO$_3$ at higher temperature, replaces the oxygen with sulfur which is also considered as a rather slow process. The conversion process was terminated after the desired optimum time for sulfurzation is also another reason that the nanowires remained intact with the substrate. The diameter of the nanowires remains the same as those fabricated at lower temperature. Few small white spots can be seen on top of the nanowires prepared at 550 °C. Thickness undulation was also noticed. Although frequent white clusters or lumps are visible throughout the wafer for the sample prepared at highest transformation temperature. These defects are related to the higher evaporation rate of the sulphur powder and faster reaction/conversion rate of oxide to sulphide. The clusters were formed by the deposition of the sulphur powder on top of the nanowires. This is obvious from the XPS survey spectra (not shown, see the Electronic Supplementary Material (ESM)) as higher amount of sulphur detected with increasing the transformation temperature. Longer conversion time also causes frequent white spot and nanowire delamination. The amount of S was 6.88 at.%, 8.37 at.% and 11.22 at.% for the nanowires fabricated at 450, 550 and 650 °C respectively.

Figure 6 (a) and (b) Cross-sectional TEM images of MoS$_2$ nanowires on Si substrate. (c) and (d) STEM and elemental mapping of MoS$_2$ nanowires respectively.
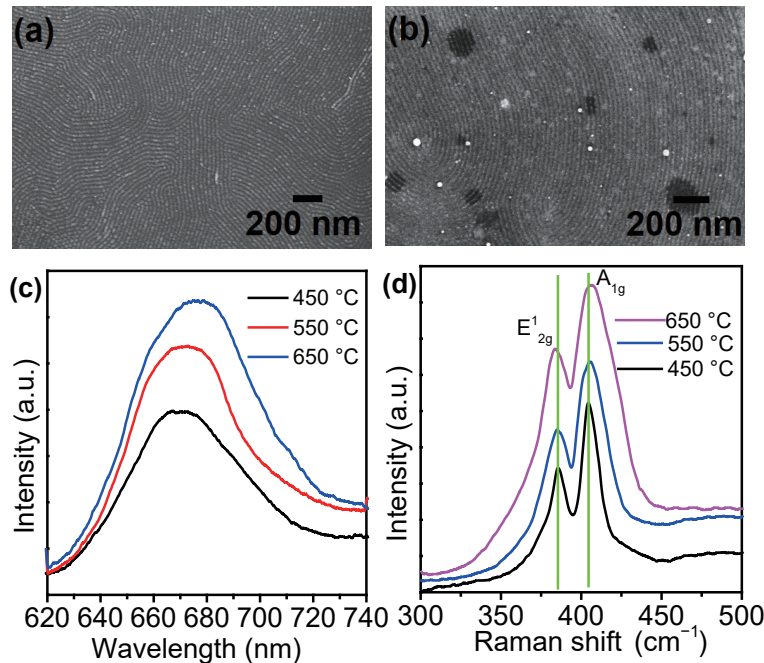
Figure 7 (a) and (b) SEM images of MoS$_2$ nanowires formed at 550 and 650 °C in an Ar/H$_2$ gas flow. (c) PL and (d) Raman spectra of MoS$_2$ nanowires formed at different temperatures.

The photoluminescence (PL) spectra were recorded for the MoS$_2$ nanowire arrays prepared at different temperatures (Fig. 7(c)). The nanowires synthesized at lowest temperature exhibit a PL peak at around 668 nm (1.85 eV) corresponding to a direct band gap transition indicating semiconducting behaviour consistent with the XPS assignment. The nanowires synthesized at higher sulfurization temperatures of 550 and 650 °C also exhibit PL peaks around 670 nm (1.85 eV) and 674 nm (1.84 eV) respectively. The peaks are broader than that synthesized at the lowest temperature, probably indicating a higher density of point defects and defect clusters. This is likely due to the formation of S vacancies in MoS$_2$. The formation of defects for the higher sulfurization temperature annealing may facilitate formation of vacancy clusters with different configurations [40]. These defects with different clustering configurations might be related to different exciton binding energies causes broadening of the observed defect related PL peaks.

High frequency mode Raman spectroscopy was carried out to confirm the 2D nature of the MoS$_2$ nanowires prepared at different temperatures (Fig. 7(d)). The spectrum shows two distinct peaks at 384 and 404 cm^{-1} for a sulfurization temperature of 450 °C, which correspond to the E$^1_{2g}$ vibrational Mo–S bond along the base plane and the A$_{1g}$ vibration of sulphur along the vertical axis, respectively [41]. The high-frequency modes, E$_{2g}$ and A$_{1g}$, shift away from each other with increasing number of layers and can be used to determine the number of individual 2D layers. The electronic structure of bulk MoS$_2$ is modified as the number of layers is reduced from few to single layers leading to a transition from indirect to direct bandgap due to increment in PL quantum yield. Also, an emission band around 680 nm becomes detectable for few-layers and is maximum for single layer MoS$_2$, and thus,

obtaining single-layer samples is crucial for most of the applications [37]. The most commonly used parameter for the direct estimate of the number of layers, N, is the frequency difference ($\Delta\omega$) between the E$_{2g}$ and A$_{1g}$, $\Delta\omega = $ A$_{1g}$ − E$_{2g}$ [42]. The nanowires prepared at lowest temperature consists of single layer corresponds to 20 cm^{-1} frequency interval [43]. Generally, E$_{2g}$ mode redshifts while A$_{1g}$ mode blueshifts with the increasing number of layers. Addition of layers increases interlayer van der Waals forces which suppress the atomic vibrations and the actively increases the force constants leads to the blueshift of A$_{1g}$ mode. While the redshift of the E$_{2g}$ mode is caused by the surface effects due to adjacent layers. The increase in the dielectric screening reduces the long-range Columbic interaction between the effective charges and thus the overall restoring forces [41]. From Fig. 7(d) it is noticed that small broadening, intensity increase and blueshift of A$_{1g}$ mode to 405 cm^{-1} and redshift of E$_{2g}$ mode to 383.5 cm^{-1} for the MoS$_2$ nanowires prepared at 550 °C corresponds to $\Delta\omega = $ 21.5 cm^{-1} for the double layers [42]. The Raman spectrum is evidently broadened and the intensity also increases for the nanowires synthesized at highest temperature. As reported in previous studies [44, 45] the presence of defects is expected for the broadening of high-frequency Raman modes as well as in activation of defect induced peaks, which is consistent with our SEM, XPS and PL studies. The measured $\Delta\omega = $ 23.5 cm^{-1} corresponds to three layers for the MoS$_2$ nanowires prepared at 650 °C.

3   Conclusions

Highly regular patterns of sub-20 nm horizontal MoS$_2$ nanowire arrays on Si substrate were fabricated using self-assembled PS-*b*-

PEO BCP line-space microphase separated arrangements. The BCP structures were achieved by a thermo-solvent approach and their morphological evolution was studied by varying the solvent annealing time. The BCP structures were etched and modified by anhydrous ethanol at 40 °C for the inclusion of molybdenum precursor within the film to form oxide nanowires maintain the BCP arrangements. Horizontal molybdenum oxide nanowires were fabricated after spin-coating precursor-ethanolic solution onto the modified template followed by UV/ozone treatment at room temperature, which led to the formation of oxide and complete removal of polymer. The conversion to sulphide was realised by thermal evaporation of sulphur powder at different temperatures in an Ar/H_2 gas flow. XPS spectra reveal the formation of MoO_3 and MoS_2 nanowires. The SEM images depict uniform diameter of the nanowires. The TEM images and elemental mapping confirm the formation of well separated oxide and sulphide nanowires on substrate surface. The nanowires have sharp elemental interfaces of Si, Mo, S and O. The formation and stability of the sulphide nanowires were investigated at different temperatures of 450, 550 and 650 °C. Frequent white spots and clusters were realized on top of the nanowires at higher temperatures. The PL spectra show a semiconducting behaviour of MoS_2 prepared at lowest temperature. The Raman spectra reveal increment of the layers of the 2D MoS_2 nanowires with increasing the sulphurization temperature. The higher temperatures reveal similar PL and Raman behaviour but the broadened spectra indicate the formation of defects and vacancy related clusters.

4 Experimental

4.1 Formation of block copolymer nanopatterns

PS-b-PEO was purchased from Polymer Source and used without further purification (number-average molecular weight, $M_n(PS)$ = 42 kg·mol⁻¹, $M_n(PEO)$ = 11.5 kg·mol⁻¹, M_w (M_w = weight-average molecular weight)/M_n = 1.07). Highly polished single-crystal silicon <100> wafers (p-type) with a native oxide layer were used as substrates without any attempt to remove the native oxide layer. Ultrasonication of the substrates in acetone and toluene separately for 30 min removed dirt, grease etc. The BCP was dissolved in toluene by stirring at room temperature to yield a 0.9 wt.% solution for at least 12 h prior to use. Thin films of BCP were formed by spin-coating the substrates at 3000 rpm for 30 s using a SCS G3P-8 spin coater. The films were exposed to toluene/THF mixed vapour with 1:1 volume ratio placed at the bottom of a closed vessel kept at a temperature of 50 °C for different time to induce microphase separation through the required chain mobility. Both horizontally and vertically aligned PEO cylinders were realized at different experimental conditions.

4.2 Fabrication of molybdenum oxide and sulphide nanowires

Partial etching and modification of the horizontal aligned PEO domain was carried out by immersing the substrate at 40 °C for 16 h in anhydrous alcohol. The substrates were then removed immediately and dried to avoid condensation onto the film surface. Following this, a molybdenum (V) chloride solution of 1 wt.% was prepared in anhydrous ethanol and spin coated onto the modified film at 3000 rpm for 30 s. UV/ozone treatment for 3 h was used to oxidize the precursor and remove the polymer. A UV/ozone system (PSD Pro Series Digital UV Ozone system; Novascan Technologies, Inc., USA) was used. The molybdenum sulphide nanowire was prepared by thermal evaporation of

sulphur in a horizontal quartz tube furnace at 450 °C for 1 h. The samples were heated at a heating rate of 15 °C·min⁻¹ under a H_2/Ar gas flow of 200 sccm. After sulfurization, samples were cooled to room temperature. The nanowires were also fabricated at different temperatures of 550 and 650 °C for 1 h and other experimental parameters were kept unchanged.

4.3 Characterization

BCP film thicknesses were measured by an optical ellipsometer (Woolam M2000). Surface morphologies were imaged by atomic force microscopy (SPM, Park systems, XE-100) in tapping mode using silicon microcantilever probe tips with a force constant of 60,000 N·m⁻¹ and a scanning force of 0.11 nN. Both topographic and phase images were recorded simultaneously. Surface morphologies were imaged by SEM (FEI Company, FEG Quanta 6700 and Zeiss Ultra Plus). Samples were prepared for TEM cross-section imaging with an FEI Helios Nanolab 600i system containing a high resolution Elstar™ Schottky field-emission SEM and a Sidewinder FIB column. TEM and elemental mapping were carried out on a FEI Titan instrument. XPS experiments was performed with an Al Kα X-ray source operating at 72 W. The high resolution core spectra peaks were deconvoluted and fitted with using Gaussian-Lorentzian function with CASA software. The PL spectra were recorded at laser excitation source wavelength of 532 nm with the beam size about 10 µm and the laser power of 0.3 mW. Each spectrum was recorded with 1 s acquisition time to avoid local overheating induced by the laser. Raman scattering spectroscopic data were collected with a Renishaw inVia Raman spectrometer using a 514 nm 30 mW argon ion laser and spectra were collected using a RenCam CCD camera. The beam was focused onto the samples using either a 20× or a 50× objective lens. Spectra were collected at different exposure time and laser intensities.

References

[1] Novoselov, K. S.; Geim, A. K.; Morozov, S. V.; Jiang, D.; Katsnelson, M. I.; Grigorieva, I. V.; Dubonos, S. V.; Firsov, A. A. Two-dimensional gas of massless Dirac fermions in graphene. *Nature* **2005**, *438*, 197–200.

[2] Zhang, Y. B.; Tan, Y. W.; Stormer, H. L.; Kim, P. Experimental observation of the quantum hall effect and Berry's phase in graphene. *Nature* **2005**, *438*, 201–204.

[3] Splendiani, A.; Sun, L.; Zhang, Y. B.; Li, T. S.; Kim, J.; Chim, C. Y.; Galli, G.; Wang, F. Emerging photoluminescence in monolayer MoS_2. *Nano Lett.* **2010**, *10*, 1271–1275.

[4] Lauritsen, J. V.; Kibsgaard, J.; Helveg, S.; Topsøe, H.; Clausen, B. S.; Lægsgaard, E.; Besenbacher, F. Size-dependent structure of MoS_2 nanocrystals. *Nat. Nanotechnol.* **2007**, *2*, 53–58.

[5] Remskar, M.; Mrzel, A.; Skraba, Z.; Jesih, A.; Ceh, M.; Demsar, J.; Stadelmann, P.; Levy, F.; Mihailovic, D. Self-assembly of subnanometer-diameter single-wall MoS_2 nanotubes. *Science* **2001**, *292*, 479–481.

[6] Kim, H. C.; Park, S. M.; Hinsberg, W. D. Block copolymer based nanostructures: Materials, processes, and applications to electronics. *Chem. Rev.* **2010**, *110*, 146–177.

[7] Mao, J.; Zhang, B. C.; Shi, Y. H.; Wu, X. F.; He, Y. Y.; Wu, D.; Jie, J. S.; Lee, C. S.; Zhang, X. H. Conformal MoS_2/silicon nanowire array heterojunction with enhanced light trapping and effective interface passivation for ultraweak infrared light detection. *Adv. Funct. Mater.* **2022**, *32*, 2108174.

[8] Mallikarjuna, K.; Shinde, M. A.; Kim, H. Electrochromic smart windows using 2D-MoS_2 nanostructures protected silver nanowire based flexible transparent electrodes. *Mater. Sci. Semicond. Process.* **2020**, *117*, 105176.

[9] Xiao, Y.; Zou, G. S.; Huo, J. P.; Sun, T. M.; Feng, B.; Liu, L. Locally thinned, core–shell nanowire-integrated multi-gate MoS_2 transistors for active control of extendable logic. *ACS Appl. Mater. Interfaces* **2023**, *15*, 1563–1573.

[10] Dieterle, G.; Mestl, M. Raman spectroscopy of molybdenum oxides. *Phys. Chem. Chem. Phys.* **2002**, *4*, 822–826.

[11] Windom, B. C.; Sawyer, W. G.; Hahn, D. W. A Raman spectroscopic study of MoS_2 and MoO_3: Applications to tribological systems. *Tribol. Lett.* **2011**, *42*, 301–310.

[12] Zhang, Z. G.; Wang, X. X.; Zhang, J.; Yu, M.; Zhang, J. C.; Zhang, H. D.; Long, Y. Z. Recent advances in 1D micro- and nanoscale indium oxide structures. *J. Alloys Compd.* **2018**, *752*, 359–375.

[13] Wang, D. W.; Sheriff, B. A.; McAlpine, M.; Heath, J. R. Development of ultra-high density silicon nanowire arrays for electronics applications. *Nano Res.* **2008**, *1*, 9–21.

[14] Cheng, J. Y.; Sanders, D. P.; Truong, H. D.; Harrer, S.; Friz, A.; Holmes, S.; Colburn, M.; Hinsberg, W. D. Simple and versatile methods to integrate directed self-assembly with optical lithography using a polarity-switched photoresist. *ACS Nano* **2010**, *4*, 4815–4823.

[15] Bates, C. M.; Bates, F. S. *50th anniversary perspective*: Block polymers-pure potential. *Macromolecules* **2017**, *50*, 3–22.

[16] Gadelrab, K. R.; Hannon, A. F.; Ross, C. A.; Alexander-Katz, A. Inverting the design path for self-assembled block copolymers. *Mol. Syst. Des. Eng.* **2017**, *2*, 539–548.

[17] Herr, D. J. C. Directed block copolymer self-assembly for nanoelectronics fabrication. *J. Mater. Res.* **2011**, *26*, 122–139.

[18] Park, C.; Yoon, J.; Thomas, E. L. Enabling nanotechnology with self assembled block copolymer patterns. *Polymer* **2003**, *44*, 6725–6760.

[19] Ghoshal, T.; Senthamaraikannan, R.; Shaw, M. T.; Holmes, J. D.; Morris, M. A. "*In situ*" hard mask materials: A new methodology for creation of vertical silicon nanopillar and nanowire arrays. *Nanoscale* **2012**, *4*, 7743–7750.

[20] Ghoshal, T.; Shaw, M. T.; Holmes, J. D.; Morris, M. A. Development of a facile block copolymer method for creating hard mask patterns integrated into semiconductor manufacturing. *Nano Res.* **2016**, *9*, 3116–3128.

[21] Rasappa, S.; Borah, D.; Faulkner, C. C.; Lutz, T.; Shaw, M. T.; Holmes, J. D.; Morris, M. A. Fabrication of a sub-10 nm silicon nanowire based ethanol sensor using block copolymer lithography. *Nanotechnology* **2013**, *24*, 065503.

[22] Chaudhari, A.; Ghoshal, T.; Shaw, M. T.; O'Connell, J.; Kelly, R. A.; Glynn, C.; O'Dwyer, C. Holmes, J. D.; Morris, M. A. Fabrication of MoS_2 nanowire arrays and layered structures via the self-assembly of block copolymers. *Adv. Mater. Interfaces* **2016**, *3*, 1500596.

[23] Mokarian-Tabari, P.; Collins, T. W.; Holmes, J. D.; Morris, M. A. Cyclical 'flipping' of morphology in block copolymer thin films. *ACS Nano* **2011**, *5*, 4617–4623.

[24] Ghoshal, T.; Chaudhari, A.; Cummins, C.; Shaw, M. T.; Holmes, J. D.; Morris, M. A. Morphological evolution of lamellar forming polystyrene-block-poly(4-vinylpyridine) copolymers under solvent annealing. *Soft Matter* **2016**, *12*, 5429–5437.

[25] Mishra, V.; Fredrickson, G. H.; Kramer, E. J. Effect of film thickness and domain spacing on defect densities in directed self-assembly of cylindrical morphology block copolymers. *ACS Nano* **2012**, *6*, 2629–2641.

[26] Zhang, X. H.; Berry, B. C.; Yager, K. G.; Kim, S.; Jones, R. L.; Satija, S.; Pickel, D. L.; Douglas, J. F.; Karim, A. Surface morphology diagram for cylinder-forming block copolymer thin films. *ACS Nano* **2008**, *2*, 2331–2341.

[27] Ghoshal, T.; Senthamaraikannan, R.; Shaw, M. T.; Holmes, J. D.; Morris, M. A. Fabrication of ordered, large scale, horizontally-aligned Si nanowire arrays based on an *in situ* hard mask block copolymer approach. *Adv. Mater.* **2014**, *26*, 1207–1216.

[28] Ghoshal, T.; Shaw, M. T.; Bolger, C. T.; Holmes, J. D.; Morris, M. A. A general method for controlled nanopatterning of oxide dots: A microphase separated block copolymer platform. *J. Mater. Chem.* **2012**, *22*, 12083–12089.

[29] Ghoshal, T.; Maity, T.; Senthamaraikannan, R.; Shaw, M. T.; Carolan, P.; Holmes, J. D.; Roy, S.; Morris, M. A. Size and space controlled hexagonal arrays of superparamagnetic iron oxide nanodots: Magnetic studies and application. *Sci. Rep.* **2013**, *3*, 2772.

[30] Ghoshal, T.; Maity, T.; Godsell, J. F.; Roy, S.; Morris, M. A. Large scale monodisperse hexagonal arrays of superparamagnetic iron oxides nanodots: A facile block copolymer inclusion method. *Adv. Mater.* **2012**, *24*, 2390–2397.

[31] Giraud, E. C.; Mokarian-Tabari, P.; Toolan, D. T. W.; Arnold, T.; Smith, A. J.; Howse, J. R.; Topham, P. D.; Morris, M. A. Highly ordered titanium dioxide nanostructures via a simple one-step vapor-inclusion method in block copolymer films. *ACS Appl. Nano Mater.* **2018**, *1*, 3426–3434.

[32] Ghoshal, T.; Ntaras, C.; Shaw, M. T.; Holmes, J. D.; Avgeropoulos, A.; Morris, M. A. A vertical lamellae arrangement of sub-16 nm pitch (domain spacing) in a microphase separated PS-b-PEO thin film by salt addition. *J. Mater. Chem. C* **2015**, *3*, 7216–7227.

[33] Choi, J. G.; Thompson, L. T. XPS study of as-prepared and reduced molybdenum oxides. *Appl. Surf. Sci.* **1996**, *93*, 143–149.

[34] Ho, S. F.; Contarini, S.; Rabalais, J. W. Metallization channels in ion-induced decomposition of molybdates and niobates. *Chem. Phys. Lett.* **1987**, *133*, 171–175.

[35] Fleisch, T. H.; Mains, G. J. An XPS study of the UV reduction and photochromism of MoO_3 and WO_3. *J. Chem. Phys.* **1982**, *76*, 780–786.

[36] Vernickaitė, E.; Lelis, M.; Tsyntsaru, N.; Pakštas, V.; Cesiulis, H. XPS studies on the Mo oxide-based coatings electrodeposited from highly saturated acetate bath. *Chemija* **2020**, *31*, 203–209.

[37] Syari'Ati, A.; Kumar, S.; Zahid, A.; Ali El Yumin, A.; Ye, J. T.; Rudolf, P. Photoemission spectroscopy study of structural defects in molybdenum disulfide (MoS_2) grown by chemical vapor deposition (CVD). *Chem. Commun.* **2019**, *55*, 10384–10387.

[38] Lee, Y.; Lee, J.; Bark, H.; Oh, I. K.; Ryu, G. H.; Lee, Z.; Kim, H.; Cho, J. H.; Ahn, J. H.; Lee, C. Synthesis of wafer-scale uniform molybdenum disulfide films with control over the layer number using a gas phase sulfur precursor. *Nanoscale* **2014**, *6*, 2821–2826.

[39] Li, B.; Jiang, L.; Li, X.; Ran, P.; Zuo, P.; Wang, A. D.; Qu, L. T.; Zhao, Y.; Cheng, Z. H.; Lu, Y. F. Preparation of monolayer MoS_2 quantum dots using temporally shaped femtosecond laser ablation of bulk MoS_2 targets in water. *Sci. Rep.* **2017**, *7*, 11182.

[40] Tongay, S.; Suh, J.; Ataca, C.; Fan, W.; Luce, A.; Kang, J. S.; Liu, J.; Ko, C.; Raghunathanan, R.; Zhou, J. et al. Defects activated photoluminescence in two-dimensional semiconductors: Interplay between bound, charged and free excitons. *Sci. Rep.* **2013**, *3*, 2657.

[41] Sam, R. T.; Umakoshi, T.; Verma, P. Probing stacking configurations in a few layered MoS$_2$ by low frequency Raman spectroscopy. *Sci. Rep.* **2020**, *10*, 21227.

[42] Cortijo-Campos, S.; Prieto, C.; De Andrés, A. Size effects in single- and few-layer MoS$_2$ nanoflakes: Impact on Raman phonons and photoluminescence. *Nanomaterials* **2022**, *12*, 1330.

[43] Buscema, M.; Steele, G. A.; Van Der Zant, H. S. J.; Castellanos-Gomez, A. The effect of the substrate on the Raman and photoluminescence emission of single-layer MoS$_2$. *Nano Res.* **2014**, *7*, 561–571.

[44] Mignuzzi, S.; Pollard, A. J.; Bonini, N.; Brennan, B.; Gilmore, I. S.; Pimenta, M. A.; Richards, D.; Roy, D. Effect of disorder on Raman scattering of single-layer MoS$_2$. *Phys. Rev. B* **2015**, *91*, 195411.

[45] Carvalho, B. R.; Wang, Y. X.; Mignuzzi, S.; Roy, D.; Terrones, M.; Fantini, C.; Crespi, V. H.; Malard, L. M.; Pimenta, M. A. Intervalley scattering by acoustic phonons in two-dimensional MoS$_2$ revealed by double-resonance Raman spectroscopy. *Nat. Commun.* **2017**, *8*, 14670.